AIAA 00-2252

Multigrid Relaxation of a Factorizable, Conservative Discretization of the Compressible Flow Equations

Thomas W. Roberts

NASA Langley Research Center

David Sidilkover

Institute for Computer Applications in Science and Engineering

and J. L. Thomas

NASA Langley Research Center

Hampton, VA

Fluids 2000

19–22 June 2000/Denver, CO

MULTIGRID RELAXATION OF A FACTORIZABLE, CONSERVATIVE DISCRETIZATION OF THE COMPRESSIBLE FLOW EQUATIONS

Thomas W. Roberts*
NASA Langley Research Center
D. Sidilkover†
Institute for Computer Applications in Science and Engineering
and J. L. Thomas‡
NASA Langley Research Center
Hampton, VA

Abstract

The second-order factorizable discretization of the compressible Euler equations developed by Sidilkover is extended to conservation form on general curvilinear body-fitted grids. The discrete equations are solved by symmetric collective Gauss-Seidel relaxation and FAS multigrid. Solutions for flow in a channel with Mach numbers ranging from 0.0001 to a supercritical Mach number are shown, demonstrating uniform convergence rates and no loss of accuracy in the incompressible limit. A solution for the flow around the leading edge of a semi-infinite parabolic body demonstrates that the scheme maintains rapid convergence for a flow containing a stagnation point.

Introduction

Steady inviscid flow is described by the Euler equations, which can be thought of as two subsystems. One subsystem corresponds to the equations governing entropy and vorticity advection. This subsystem is hyperbolic in space. The other subsystem corresponds to a full potential operator, which is elliptic for subsonic flow and hyperbolic for supersonic flow. For a purely supersonic flow, space marching is the most efficient way of solving the Euler equations. For subsonic flow, the ellipticity of the full potential factor should be effectively handled by multigrid. However multigrid is not effective for advection operators, as the coarse grid only gives part of the correction for certain smooth components of the error. Existing multigrid methods for subsonic and transonic flow rely on the coarse grid to smooth the entire system. As such, they are fundamentally limited by the ineffectiveness of the coarse grid in correcting the part of the error corresponding to advection factor. This same difficulty is true for high Reynolds-number viscous flows as well.

As has been pointed out by Brandt[1], to obtain ideal multigrid convergence rates for subsonic, inviscid flows, the discretization must distinguish those parts of the differential operator which correspond to advection, and those which correspond to elliptic behavior. The advection terms are treated efficiently by marching and the elliptic terms are rapidly solved with a multigrid iteration. Brandt[1] argues that by splitting the system into its elliptic and advection parts, the convergence rate of the full system ought to be equal to the slowest of the two subsystems. Using this approach, Brandt and Yavneh have demonstrated textbook multigrid for the incompressible Navier-Stokes equations[2]. Their results are for a simple geometry and a Cartesian grid, using a staggered-grid discretization of the equations. In a closely related approach, Ta'asan[3] presented a fast multigrid solver for the compressible Euler equations. This method is based on a set of "canonical variables" which express the steady Euler equations in terms of an elliptic and a hyperbolic partition[4]. In Reference 3 it is shown that ideal multigrid efficiency can be achieved for the compressible Euler equations for two-dimensional subsonic flow using body-fitted grids.

In an earlier work[5, 6], the authors presented a multigrid scheme for the steady, incompressible Euler equations based on a pressure Poisson discretization which distinguishes the advection operator from the elliptic part of the system of equations. Both structured grid and unstructured grid flow solvers were written using the discretization. The results in Ref. 5 demonstrated that the scheme can achieve ideal multigrid convergence rates for internal flows. The scheme has been extended to three dimensions by Sanchez[7], who has also demonstrated ideal multigrid convergence rates for internal flows. This approach has the advantage of non-staggered grids -- a collocated, vertex-based discretization of the equations is used, simplifying the restriction and prolongation operations and allowing the use of simple point collective Gauss-Seidel relaxation. Although the pres-

* Research Scientist
† Senior Staff Scientist
‡ AIAA Fellow

sure Poisson approach may be extended to compressible flows, it is not conservative and is unsuited for supercritical flows with shocks. Furthermore, the extension to viscous flows is limited to the incompressible Navier-Stokes equations.

Recently, Sidilkover[8] has devised a discretization of the compressible flow equations that overcomes these limitations. This discretization may be applied to the Euler equations in conservative form, using the multidimensional upwind scheme of Sidilkover[9, 10]. In Ref. 10 it is shown that this approach should lead to a scheme that is *factorizable*, i.e., the scheme distinguishes between those parts of the operator that represent advection, and that part of the operator that represents potential flow. In Ref. 8, such a factorizable scheme is constructed for Cartesian grids. Because the discretization is stable for Gauss-Seidel relaxation, it the convergence rate does not depend upon a Courant-Friedrich-Lewy number restriction, unlike standard discretizations of the Euler equations which must use time marching. For this reason, the same convergence rate is obtained for subsonic Mach numbers all the way to the incompressible limit. The scheme may be written in the form of a central-difference part plus an artificial viscosity. As such, it is very similar in formulation to standard upwind, finite-volume discretizations for the Euler and Reynolds-Averaged Navier-Stokes equations, and can be written as a conventional upwind scheme with a modified artificial dissipation. Sidilkover[8] shows that for the discrete scheme to preserve factorizability the dissipation terms must be discretized in a specific way. In addition, he shows that the artificial viscosity may be rescaled with the Mach number such that the factorizability, and thus the accuracy, as well as the h-ellipticity of the operator is preserved in the incompressible limit.

In the present work, the generalization of Sidilkover's factorizable scheme to curvilinear, body-fitted coordinates is presented. First, the governing equations are presented, including the form of the multidimensional upwind artificial dissipation. It is shown how the dissipation terms must be discretized to maintain factorizability. A discussion of the point collective Gauss-Seidel relaxation is presented next. Solutions for flow in a channel, with inlet Mach numbers ranging from 0.0001 to a supercritical Mach number are shown, demonstrating the accuracy and convergence rates of the scheme. An additional computation for the flow around the leading edge of a semi-infinite parabola demonstrates that the current scheme does not suffer from the convergence difficulties near a stagnation point that were observed for the authors' previous scheme [11].

Mathematical Formulation

The artificial dissipation of the factorizable scheme can be described by first presenting the modified equation, or first differential approximation (FDA), of the discrete scheme. This is the differential equation which is found by expanding the difference equation in a Taylor series about each grid vertex and considering the leading terms of the truncation error. These terms are the artificial dissipation of the scheme.

The starting point for the scheme is the two-dimensional Euler equations in non-conservation form. Let ρ be the density, $\vec{u} = \hat{\imath}u + \hat{\jmath}v$ be the velocity, and p be the pressure. The entropy s is defined as

$$s \equiv \left(\frac{p}{p_0}\right)\left(\frac{\rho}{\rho_0}\right)^{-\gamma}, \tag{1}$$

where p_0 and ρ_0 are a reference pressure and density, respectively, and γ is the ratio of the specific heats. Then the Euler equations may be written in the variables (s, u, v, p):

$$\vec{u}\cdot\nabla s = 0, \tag{2a}$$

$$\vec{u}\cdot\nabla\vec{u} + \frac{1}{\rho}\nabla p = 0, \tag{2b}$$

$$\rho c^2 \nabla\cdot\vec{u} + \vec{u}\cdot\nabla p = 0. \tag{2c}$$

The factorizability of the scheme depends on the form of the artificial dissipation added to this system of equations.

The entropy is only weakly coupled to the momentum and the pressure equations through the equation of state (1). In fact, the entropy equation corresponds to one of the advection factors of the Euler equations. Therefore, it may be discretized independently of the momentum and pressure equations in any appropriate way without affecting the factorizability of the scheme. The advection operator $\vec{u}\cdot\nabla$ uses simple upwind differencing in Eq. (2a). Let (ξ, η) be a general curvilinear coordinate system and define the contravariant components of the velocity, $(\bar{U}, \bar{V})$ by the transformation

$$\begin{pmatrix} x_\xi & x_\eta \\ y_\xi & y_\eta \end{pmatrix}\begin{pmatrix} \bar{U} \\ \bar{V} \end{pmatrix} = \begin{pmatrix} u \\ v \end{pmatrix}. \tag{3}$$

In this coordinate system $\vec{u}\nabla\vec{u} = \bar{U}\partial_\xi + \bar{V}\partial_\eta$. The equations are discretized on a uniform grid in (ξ, η) space, with a grid spacing $\Delta\xi = \Delta\eta = 1$. The FDA of the first-order upwind difference approximation to $\vec{u}\cdot\nabla$ is

$$\mathbf{q} \equiv \vec{u}\cdot\nabla - \frac{1}{2}\left|\bar{U}\right|\partial_\xi^2 - \frac{1}{2}\left|\bar{V}\right|\partial_\eta^2 = 0, \tag{4}$$

and the entropy equation is discretized as

$$\mathbf{q}s = 0. \tag{5}$$

A second-order upwind discretization of the advection operator has also been used in Eq. (5). However, for the particular cases shown below the use of a second-order advection operator has an insignificant affect on the computed results. This point is discussed in the Results section.

The dissipation for the momentum and pressure equations, Eqs. (2b) and (2c), is the multidimensional upwind

dissipation of Sidilkover[9]. In vector notation, this dissipation is written as

$$\vec{u}\cdot\nabla\vec{u} + \frac{1}{\rho}\nabla p - \frac{\sigma_m \ell}{2\rho c}\nabla\left(\rho c^2 \nabla\cdot\vec{u} + \vec{u}\cdot\nabla p\right) = 0, \quad (6)$$

$$\rho c^2 \nabla\cdot\vec{u} + \vec{u}\cdot\nabla p - \rho c \frac{\sigma_p \ell}{2}\nabla\cdot\left(\vec{u}\cdot\nabla\vec{u} + \frac{1}{\rho}\nabla p\right) = 0, \quad (7)$$

where c is the speed of sound, σ_m and σ_p are scaling coefficients, and ℓ is a length scale proportional to the grid spacing. Note that the dissipation of the momentum equation is the gradient of the pressure equation residual, and the dissipation of the pressure equation is the divergence of the momentum equation residual. It is this property of the artificial dissipation that leads to a factorizable scheme. Note that the curl of Eq. (6) is identical to the curl of Eq. (2b), i.e., vorticity equation of the governing Euler equations is unaffected by the artificial dissipation. The vorticity equation corresponds to the second advection factor of the Euler equations. Similarly, because the dissipation of Eq. (7) is the divergence of the momentum equation, it is affected only by the irrotational part of the velocity field but not the solenoidal part. The irrotational part may be written as the gradient of a potential. As the pressure equation Eq. (2c) is a form of the continuity equation, it corresponds to the full potential factor, and the FDA described by Eq. (7) preserves this property.

If the advection operator, pressure gradient, and divergence terms in Eqs. (6) and (7) are discretized using central differences, the scheme is second-order accurate and factorizable. However, such a scheme is not h-elliptic. This lack of h-ellipticity is a result of the central difference approximation to the advection term in the momentum equation, Eq. (6). Sidilkover shows that this advection operator corresponds to vorticity advection[8]. Replacing this operator by the first-order upwind approximation in Eq. (4) restores h-ellipticity and the scheme remains factorizable, but it now becomes only first-order accurate. Note that the pressure advection term in Eq. (7) continues to be approximated by second-order central differences.

To obtain second-order accuracy while maintaining h-ellipticity, appropriate antidissipative terms must be added to the momentum equation in such a way that factorizability is preserved. The form of these terms is dependent upon the computational coordinates (ξ, η), and they must be written in terms of the contravariant and covariant components of the velocity vector. The covariant components are related to the physical components by the transformation

$$\begin{pmatrix} x_\xi & y_\xi \\ x_\eta & y_\eta \end{pmatrix}\begin{pmatrix} u \\ v \end{pmatrix} = \begin{pmatrix} \bar{U} \\ \bar{V} \end{pmatrix}. \quad (8)$$

Writing the advection operator in Eq. (6) in terms of the covariant velocity components and ignoring terms containing the higher-order geometric derivatives, the scheme may be upgraded to nearly second-order by adding the following corrections:

$$\vec{u}\cdot\nabla\bar{U} = \mathbf{q}\bar{U} + \frac{1}{2}\left|\bar{U}\right|\partial_\xi^2\bar{U} + \frac{1}{2}\left|\bar{V}\right|\partial_\xi\partial_\eta\bar{V}, \quad (9a)$$

$$\vec{u}\cdot\nabla\bar{V} = \mathbf{q}\bar{V} + \frac{1}{2}\left|\bar{U}\right|\partial_\xi\partial_\eta\bar{U} + \frac{1}{2}\left|\bar{V}\right|\partial_\eta^2\bar{V}. \quad (9b)$$

The cross-derivative terms in Eq. (9) are necessary for second-order accuracy and to retain factorizability at the same time. Using Eq. (8) to find $\bar{U}$ and $\bar{V}$, the antidissipative terms in Eq. (9a) and (9b) are evaluated, and then rotated back into the physical components. This gives a discretization of the form

$$\vec{u}\cdot\nabla\vec{u} = \mathbf{q}\vec{u} + \nabla D \quad (10)$$

where

$$D \equiv \frac{1}{2}\left(\left|\bar{U}\right|\partial_\xi\bar{U} + \left|\bar{V}\right|\partial_\eta\bar{V}\right). \quad (11)$$

The above expression is the generalization to curvilinear coordinates of the one given in Ref. 8.

To gain more insight about the nature of the correction terms, the FDA of Eq. (10) may be rewritten as

$$\mathbf{q}\vec{u} + \nabla D = \vec{u}\cdot\nabla\vec{u} + \frac{J}{2}\left(\vec{e}^{\,\xi}\left|\bar{V}\right|\partial_\eta\omega - \vec{e}^{\,\eta}\left|\bar{U}\right|\partial_\xi\omega\right)$$

where $\omega \equiv \partial_x v - \partial_y u$ is the vorticity, $J \equiv x_\xi y_\eta - y_\xi x_\eta$ is the Jacobian of the coordinate transformation, and $(\vec{e}^{\,\xi}, \vec{e}^{\,\eta})$ are the contravariant basis vectors in the (ξ, η) coordinate directions.* Note that if the flow is irrotational, then the first-order truncation error terms vanish identically and the approximation becomes second-order accurate.

It was pointed out above that factorizability depends upon the dissipation of the momentum equation being written as the gradient of the pressure equation, and the dissipation of the pressure equation being written as the divergence of the momentum equation. Likewise, the second-order correction to the advection terms must be in the form of a gradient so that the vorticity equation is is unaffected. With the definition in Eq. (10), taking the curl of Eq. (6) yields $\mathbf{q}\omega = 0$. Thus the advection operator acting on the vorticity is unchanged from the first-order scheme.

To get full second-order accuracy it is necessary to use second-order accurate discretization of the advection operator in the momentum equation. The FDA of an h-elliptic, fully second-order upwind advection operator

$$\mathbf{q}_{\mathrm{HO}} = \bar{U}\partial_\xi + \bar{V}\partial_\eta - \frac{1}{2}\left(\left|\bar{U}\right|\partial_\xi^2 + 2\,\mathrm{sgn}\bar{U}\,\bar{V}\partial_\xi\partial_\eta + \frac{\bar{V}^2}{\left|\bar{U}\right|}\partial_\eta^2\right) \quad (12a)$$

when $\left|\bar{U}\right| > \left|\bar{V}\right|$ and

$$\mathbf{q}_{\mathrm{HO}} = \bar{U}\partial_\xi + \bar{V}\partial_\eta - \frac{1}{2}\left(\frac{\bar{U}^2}{\left|\bar{V}\right|}\partial_\xi^2 + 2\,\mathrm{sgn}\bar{V}\,\bar{U}\partial_\xi\partial_\eta + \left|\bar{V}\right|\partial_\eta^2\right) \quad (12b)$$

*$J\vec{e}^{\,\xi} = iy_\eta - jx_\eta$, $J\vec{e}^{\,\eta} = -iy_\xi + jx_\xi$

when $|\bar{U}| < |\bar{V}|$. With this advection operator in the momentum equation, the quantity D in Eq. (11) must be modified in order to preserve the factorizability of the scheme. This modified D is given by

$$D_{\mathrm{HO}} \equiv D + \frac{1}{2}\mathrm{sgn}\bar{U}\,\bar{V}\,(\partial_\eta \bar{U} + \partial_\xi \bar{V}) - \frac{1}{2}|\bar{V}|\left(1 - \left|\frac{\bar{V}}{\bar{U}}\right|\right)\partial_\eta \bar{V} \quad (13a)$$

when $|\bar{U}| > |\bar{V}|$ and

$$D_{\mathrm{HO}} \equiv D + \frac{1}{2}\mathrm{sgn}\bar{V}\,\bar{U}\,(\partial_\eta \bar{U} + \partial_\xi \bar{V}) - \frac{1}{2}|\bar{U}|\left(1 - \left|\frac{\bar{U}}{\bar{V}}\right|\right)\partial_\xi \bar{U} \quad (13b)$$

when $|\bar{U}| < |\bar{V}|$. Taking the curl of the momentum equation now gives $\mathbf{q}_{\mathrm{HO}}\,\omega = 0$, i. e., the vorticity equation is now second-order accurate.

To see how the multidimensional upwind dissipation of Eqs. (6), (7) and (9) is related to the standard first-order upwind difference scheme, consider a uniform Cartesian grid with equal spacing in the x and y directions. If the scaling coefficients σ_m and σ_p are taken to be one, ℓ is the grid spacing, and the cross-derivative terms in the dissipation terms of Eqs. (6) and (7) are ignored, the standard first-order upwind scheme is obtained. The first-order upwind scheme on a nonuniform grid further replaces $\ell\nabla$ by $\ell_x\partial_x + \ell_y\partial_y$, where ℓ_x and ℓ_y are the grid spacings in the two coordinate directions. The multidimensional upwind scheme uses a single length scale, and retains the cross-derivative terms. Consider the advection operator of Eq. (9) on a Cartesian grid. Dropping the cross-derivative terms yields the standard first-order upwind discretization.

Discretization

The factorizability of the FDA is a necessary condition for the factorizability of the difference scheme, but it is not sufficient. For the difference scheme to be factorizable, the difference operators must commute in the same way as the differential operators[8]. Introducing the difference approximations to the partial derivative operators,

$$\partial_\xi^h = \partial_\xi + \cdots, \qquad \partial_\eta^h = \partial_\eta + \cdots,$$
$$\partial_{\xi\xi}^h = \partial_\xi^2 + \cdots, \qquad \partial_{\eta\eta}^h = \partial_\eta^2 + \cdots,$$
$$\partial_{\xi\eta}^h = \partial_\xi\partial_\eta + \cdots,$$

the following conditions must hold

$$\partial_{\xi\xi}^h\partial_{\eta\eta}^h = \partial_{\xi\eta}^h\partial_{\xi\eta}^h$$
$$\partial_{\xi\xi}^h\partial_\eta^h = \partial_{\xi\eta}^h\partial_\xi^h,$$
$$\partial_{\eta\eta}^h\partial_\xi^h = \partial_{\xi\eta}^h\partial_\eta^h.$$

The following difference operators satisfy this condition:

$$\bar{\partial}_\xi^h = \frac{1}{8}\begin{bmatrix}-1 & 0 & 1\\ -2 & 0 & 2\\ -1 & 0 & 1\end{bmatrix}, \quad \bar{\partial}_\eta^h = \frac{1}{8}\begin{bmatrix}1 & 2 & 1\\ 0 & 0 & 0\\ -1 & -2 & -1\end{bmatrix},$$
$$\bar{\partial}_{\xi\xi}^h = \frac{1}{4}\begin{bmatrix}1 & -2 & 1\\ 2 & -4 & 2\\ 1 & -2 & 1\end{bmatrix}, \quad \bar{\partial}_{\eta\eta}^h = \frac{1}{4}\begin{bmatrix}1 & 2 & 1\\ -2 & -4 & -2\\ 1 & 2 & 1\end{bmatrix},$$
$$\bar{\partial}_{\xi\eta}^h = \frac{1}{4}\begin{bmatrix}-1 & 0 & 1\\ 0 & 0 & 0\\ 1 & 0 & -1\end{bmatrix}.$$

To write the complete discrete scheme, the subscript h is used to denote a standard difference to the corresponding operator, and the addition of the overbar $\bar{(\ )}$ denotes the "wide" differences given above. The second-difference expressions may be expressed in flux form by taking a six-point difference centered on an edge between two vertices, and then taking a two-point difference of those expressions centered on a vertex. The subscripts e and v are used to denote difference operators centered on an edge or a vertex, respectively. The fully discrete scheme is then written as

$$\mathbf{q}^h s = 0, \quad (14a)$$

$$\mathbf{q}_{\mathrm{HO}}^h\vec{u} + \nabla_v D_{\mathrm{HO}}^h + \frac{1}{\rho}\bar{\nabla}^h p - \frac{\sigma_m\ell}{2\rho c}\nabla_v^h\left(\rho c^2\bar{\nabla}_e^h\cdot\vec{u} + \vec{u}\cdot\bar{\nabla}_e^h p\right) = 0, \quad (14b)$$

$$\rho c^2\nabla^h\cdot\vec{u} + \vec{u}\cdot\bar{\nabla}^h p - \rho c\frac{\sigma_p\ell}{2}\nabla_v^h\cdot\left(\vec{u}\cdot\nabla_e^h\vec{u} + \frac{1}{2\rho}\left(\nabla_e^h + \bar{\nabla}_e^h\right)p\right) = 0. \quad (14c)$$

The derivatives in that part of D_{HO} given in Eq. (11) are discretized using the wide, six-point difference stencil for $\partial_\xi^h\bar{U}$ and $\partial_\eta^h\bar{V}$. The additional terms of D_{HO} and the corresponding dissipation terms for the second-order advection operator $\mathbf{q}_{\mathrm{HO}}$ must be discretized in a very precise way, and depend upon the flow direction and the relative magnitudes of $\bar{U}$ and $\bar{V}$. The details are described in Ref. 12 for uniform Cartesian grids. The stencils for the general curvilinear grids are presented in the appendix to this paper.

The scaling coefficients are

$$\sigma_m = \max(M, M_c), \qquad \sigma_p = \frac{1}{\max(M, M_c)} \quad (15)$$

where M is the local Mach number, and M_c is a cutoff Mach number to prevent division by zero. The cutoff is chosen to be $O(h)$, and essentially becomes active near stagnation points. The purpose of the rescaling of the pressure equation dissipation, σ_p, is to prevent the elliptic factor in the discrete equations from becoming the skewed Laplacian operator in the incompressible limit.

Currently, we take $M_c = \nu|\Delta M|$, where $\nu = 5$ and ΔM is the two-point difference in Mach number on an edge. For the channel flow cases shown below, M_c never becomes larger than M. For the leading-edge flow, the cutoff does become active at the stagnation point. When $M_c > M$, it is necessary to add additional dissipation to the advection operator $\mathbf{q}^h_{\rm HO}$. The form of this dissipation is a five-point pseudo-Laplacian,

$$d_{\rm sp} = \frac{1}{2}\max(0, M_c - M)\frac{c\ell}{J}\left(\partial_\xi^2 + \partial_\eta^2\right), \qquad (16)$$

where J is the Jacobian of the coordinate transformation. This operator is added to both the entropy and the momentum equation, and is cast in flux form in order to maintain conservation. No attempt has been made to optimize either the coefficient ν or the form of the operator $d_{\rm sp}$.

As written, the Eq. (14) is valid only for subsonic flows. This is because the pressure differences in the artificial dissipation terms are not fully upwinded in a supersonic zone. A simple modification to Eq. (14) can be made by rescaling the gradients of the pressure when the flow becomes sonic. Introducing the parameter κ, defined as

$$\kappa = \max(1, M^2), \qquad (17)$$

the final form of the scheme is

$$\mathbf{q}^h s - d_{\rm sp} s = 0, \qquad (18a)$$

$$\mathbf{q}^h_{\rm HO}\vec{u} - d_{\rm sp}\vec{u} + \nabla_v D^h_{\rm HO} + \frac{1}{\rho}\bar{\nabla}^h p - \frac{\sigma_m \ell}{2\rho c}\nabla^h_v\left(\rho c^2 \bar{\nabla}^h_e\cdot\vec{u} + \frac{1}{\kappa}\vec{u}\cdot\bar{\nabla}^h_e p\right) = 0, \qquad (18b)$$

$$\rho c^2 \nabla^h\cdot\vec{u} + \vec{u}\cdot\bar{\nabla}^h p - \rho c\frac{\sigma_p\ell}{2}\nabla^h_v\cdot\left(\vec{u}\cdot\nabla^h_e\vec{u} + \frac{\kappa}{2\rho}\left(\nabla^h_e + \bar{\nabla}^h_e\right)p\right) = 0. \qquad (18c)$$

Because the difference equations (14a), (14b) and (14c), can be written as a central difference part plus a dissipation, it is straightforward to obtain a conservative discretization. The conservation form of the Euler equations are discretized using a central-difference finite-volume approximation,

$$\nabla^h\cdot(\rho\vec{u}) = 0, \qquad (19a)$$

$$\nabla^h\cdot(\rho\vec{u}\vec{u}) + \nabla^h p = 0, \qquad (19b)$$

$$\nabla^h\cdot[(\rho e + p)\vec{u}] = 0 \qquad (19c)$$

where $e = \vec{u}\cdot\vec{u}/2 + p/(\rho(\gamma - 1))$ is the total energy. The dissipative fluxes on each cell face are computed in terms of (s, u, v, p) using the appropriate difference operators in Eq. (14). The artificial dissipation in Eqs. (14b) and (14c) can be rewritten as

$$\delta\vec{u} = -\nabla_v D^h_{\rm HO} + d_{\rm sp}\vec{u} + \nabla^h_v\left[\frac{\sigma_m\ell}{2}\left(c\bar{\nabla}^h_e\cdot\vec{u} + \frac{1}{\rho c\kappa}\vec{u}\cdot\bar{\nabla}^h_e p\right)\right], \qquad (20)$$

$$\delta p = \nabla^h_v\cdot\left[\frac{\sigma_p\ell}{2}\left(\rho c\vec{u}\cdot\nabla^h\vec{u} + \frac{c\kappa}{2}\left(\nabla^h_e + \bar{\nabla}^h_e\right)p\right)\right]. \qquad (21)$$

This is a conservative form of the dissipation cast in terms of the primitive variables. The terms inside the square bracket in Eqs. (20) and (21) are now interpreted as dissipative fluxes. These terms are discretized on cell faces according to the appropriate wide or narrow differences. The first-order upwind advection operator $\mathbf{q}^h$ and the antidissipative terms $\vec{D}^h(\bar{U}, \bar{V})$ in Eq. (20) may be recast in conservation form and evaluated on cell faces. The length scale ℓ is evaluated on the cell face by taking $\min(\ell_\xi, \ell_\eta)$, the shortest length in each grid direction. The scaling coefficients σ_m and σ_p are evaluated using the Mach number on the face.

In addition to the dissipation terms, examination of Eqs. (14b) and (14c) shows that the pressure gradient terms are discretized using the wide stencils. The central-difference part of the conservation equations (19) must be corrected to account for these wide differences. This is done by adding a term to the dissipative fluxes for the momentum and pressure equations as follows:

$$\delta\vec{u} \leftarrow \delta\vec{u} - \frac{1}{\rho}\left(\bar{\nabla}^h - \nabla^h\right)p, \qquad (22)$$

$$\delta p \leftarrow \delta p - \vec{u}\cdot\left(\bar{\nabla}^h - \nabla^h\right)p. \qquad (23)$$

Once the dissipative fluxes $(\delta s, \delta u, \delta v, \delta p)$ have been evaluated, they are converted to the conservation variables by the transformation

$$\begin{pmatrix}\delta\rho\\ \delta\rho u\\ \delta\rho v\\ \delta\rho e\end{pmatrix} = \begin{pmatrix}-\rho/s & 0 & 0 & 1/c^2\\ -\rho u/s & \rho & 0 & u/c^2\\ -\rho v/s & 0 & \rho & v/c^2\\ -\rho(u^2+v^2)/2s & \rho u & \rho v & h/c^2\end{pmatrix}\begin{pmatrix}\delta s\\ \delta u\\ \delta v\\ \delta p\end{pmatrix}, \qquad (24)$$

where $h = e + p/\rho$ is the total enthalpy.

Solution Procedure

The solution of the discrete equations is performed using a symmetric point collective Gauss-Seidel iteration, which has been found to be a very effective smoother. The grid points are ordered such that the forward Gauss-Seidel sweep is in the streamwise direction. This means that the entropy equation is marched in space during the forward sweep. The reverse Gauss-Seidel sweep is underrelaxed with a factor of 0.5 for stability. The residuals of the conservation equations $(r_\rho, r_{\rho u}, r_{\rho v}, r_{\rho e})$ are computed at each vertex using the discretization presented in the previous section. These residuals are then transformed to the residuals of the primitive variables by the inverse of the transformation in Eq. (24).

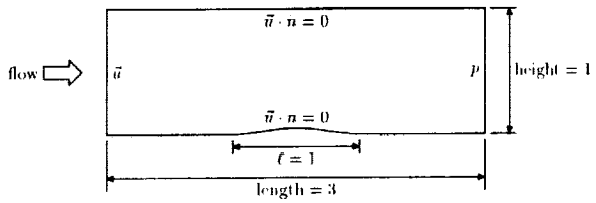

Figure 1. Channel geometry.

At each point, the update to the solution is given by

$$\mathbf{M} \begin{pmatrix} \Delta s \\ \Delta u \\ \Delta v \\ \Delta p \end{pmatrix}_{i,j} = - \begin{pmatrix} r_s \\ r_u \\ r_v \\ r_p \end{pmatrix}_{i,j} \tag{25}$$

where $\mathbf{M}$ is the matrix of coefficients of the primitive variables at vertex (i, j). The coefficients are found by collecting the contributions to vertex (i, j) from the dissipation terms on the four surrounding faces. Because the entropy equation decouples from the rest of the system, this is a block diagonal matrix where the upper block is the upper left-hand entry, and the lower block is a 3×3 matrix of coefficients multiplying $u_{i,j}$, $v_{i,j}$, and $p_{i,j}$. This matrix is easily inverted.

The relaxation is accelerated using a standard Full-Approximation Scheme (FAS) multigrid. A sequence of grids $G_K, G_{K-1}, \ldots, G_0$ is used, where G_K is the finest and G_0 the coarsest. Let $\tilde{\mathbf{L}}_{k-1}$ be the coarse grid operator, $\mathbf{u}$ be the vector of the conservation variables, I_{k-1}^k be the fine-to-coarse grid restriction operator, and I_k^{k-1} be the coarse-to-fine grid prolongation operator. If $\hat{\mathbf{u}}_k$ is the current solution on grid k, the residual on this grid is $\mathbf{r}_k \equiv \mathbf{f}_k - \tilde{\mathbf{L}}_k \hat{\mathbf{u}}_k$. This is the residual of the conservation equations, not the primitive equations. This leads to the coarse-grid equation

$$\tilde{\mathbf{L}}_{k-1} \hat{\mathbf{u}}_{k-1} = \mathbf{f}_{k-1} = I_{k-1}^k \mathbf{r}_k + \tilde{\mathbf{L}}_{k-1} \left(I_{k-1}^k \hat{\mathbf{u}}_k \right). \tag{26}$$

After solving the coarse-grid equation for $\mathbf{u}_{k-1}$, the fine-grid solution is corrected by

$$\hat{\mathbf{u}}_k^{\text{new}} \leftarrow \hat{\mathbf{u}}_k + I_k^{k-1} \left(\hat{\mathbf{u}}_{k-1} - I_{k-1}^k \hat{\mathbf{u}}_k \right). \tag{27}$$

Equation (26) is solved by applying the same relaxation procedure that is used to solve the fine-grid equation. Multigrid is applied recursively to the coarse-grid equation. On the coarsest grid, many relaxation sweeps are performed to insure that the equation is solved completely. A conventional V cycle or W-cycle is used.

Results

Solutions are shown for compressible flow in a two-dimensional channel, the geometry of which is shown in Fig. 1. The shape of the lower wall between $0 \le x \le 1$ is $y(x) = \tau \sin^2 \pi x$. For the computations shown here, the thickness ratio τ is 0.05. The grid spacing is uniform in the x-direction, and the coordinates in the y-direction are found using a simple shearing transformation.

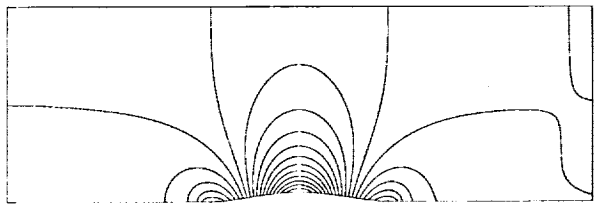

Figure 2. Mach number contours for a $M = 0.5$ inlet, contour increment $\Delta M = 0.01$, for a 385×129 grid.

At the inflow boundary the entropy, total enthalpy and flow angle are specified, and the pressure is extrapolated from the interior. The outflow boundary condition is a specified pressure and s, u and v are extrapolated from the interior. At the upper and lower walls of the channel, the flow tangency condition $\vec{u} \cdot \hat{n} = 0$ is enforced by setting the residual of the momentum equation normal to the wall to zero. Because of the wide stencils the dissipation terms on the wall are evaluated using a row of ghost vertices. The pressure is extrapolated to those vertices using the normal momentum equation. The entropy and total enthalpy at the ghost vertices are set to the values on the wall, and the normal component of the velocity is reflected from the interior.

Solutions are obtained using a FMG cycle to initialize the solution. A solution is computed on the coarsest grid and prolonged to the next grid to obtain a starting solution for that grid. This procedure is continued recursively until the finest grid is reached. On each grid, a $V(1, 1)$ multigrid cycle is used to solve the system. Five multigrid cycles are run on each of the coarse grids, and fifteen cycles are run on the finest grid. After each symmetric Gauss-Seidel relaxation sweep, an additional three streamwise sweeps are done on the wall and its neighboring row of vertices.

Mach contours are seen in Fig. 2 on a 385×129 fine grid for an inlet Mach number of 0.5. The solution is symmetric except for a glitch at the outflow boundary, which is caused by specifying uniform pressure at the outflow boundary. Convergence rates are shown in Fig. 3. A total of 7 grids is used, the coarsest being 7×3. The residual levels are renormalized after each prolongation to the next finest grid, and on the coarsest grid several relaxation sweeps are performed, giving essentially a direct solve on that grid. The convergence rate on the finest grid is initially 0.25 per $V(1, 1)$ cycle, and the asymptotic rate is 0.38 per cycle. The residual reduction over 5 cycles is seen to be the same on each grid, showing that the convergence rate is $O(n)$. The drag on the lower wall and the rms error in the entropy over the computational domain are shown in Fig. 4. On the finest

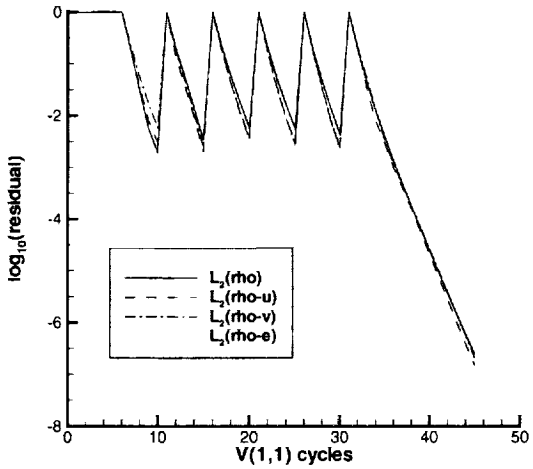

Figure 3. Convergence rates for a $M = 0.5$ inlet flow using a FMG cycle with a 385×129 fine grid.

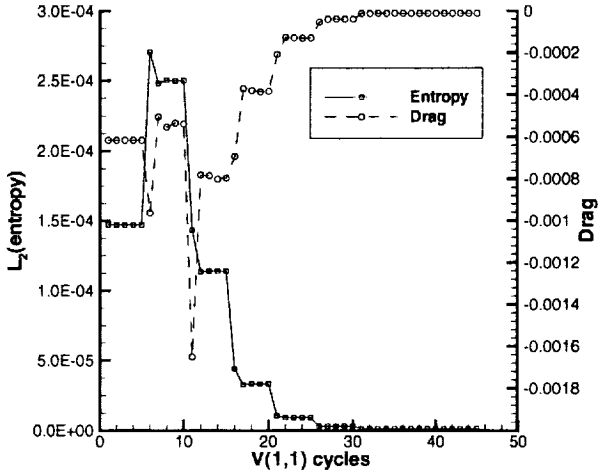

Figure 4. Convergence of the L_2 entropy error and drag on the lower wall for a $M = 0.5$ inlet flow using a FMG cycle with a 385×129 fine grid.

grids both are converged after essentially two multigrid cycles.

The drag and entropy appear to be exhibiting better than first-order accuracy but not quite second-order accuracy. On the finer grids, the error decreases by approximately one-third with the halving of the grid spacing. The entropy error decreases by about 0.28 on the finest grids, while the drag is reduced by about 0.35. These values are somewhat sensitive to the choice of the wall boundary condition. Curiously, when simple reflection boundary conditions are used, the drag converges better than second order, dropping by a factor of six to eight with each grid refinement. Neither the drag nor the entropy is very sensitive to whether a first-order or a second-order advection operator is used in either Eq. (18a) or Eq. (18b). This is because the flow is a potential flow, and the factorizability of the scheme decouples the entropy and vorticity advection from the potential factor of the operator. Given that s and ω are identically zero analytically, first-order advection is perfectly adequate.

To demonstrate that the factorizable scheme requires no special preconditioning to handle very low Mach numbers, a solution for an inlet Mach number of 10^{-4} is shown in Figs. 5, 6 and 7. Because the ratio of the dynamic pressure to the static pressure is $O(M^2)$, the relative roundoff error is much larger for this case than for the higher Mach number cases, so the residuals bottom out at a higher level. The initial convergence rate is 0.24 per cycle, very close to that for the Mach number 0.5 case. As with the higher Mach number case, the convergence rate is $O(n)$. The solution is seen to be very symmetrical at the bump, with some boundary layer behavior at the inflow and the same behavior at the outflow as for the the higher Mach number. The drag and entropy errors converge within two cycles on the finest grids.

Mach contours, residual convergence and the drag and entropy are shown in Figs. 8, 9 and 10 for an inlet Mach number of 0.73, which corresponds to a supercritical inlet Mach number. The peak Mach number before the shock is approximately 1.2. The rate of residual reduction is initially about 0.53 per cycle on the 385×129 fine grid, and the asymptotic rate is 0.68. The drag and entropy take longer to converge than for the subcritical cases, and in fact they have not converged on any of the coarse grids before the solution is interpolated to the next finer grid. On the finest grid, the drag and entropy converge in about eight cycles.

All the solutions shown so far do not have a stagnation point. In earlier work, the pressure Poisson scheme of Roberts, Sidilkover and Swanson[5, 6] exhibited a deterioration in the convergence rate for flows containing a stagnation point[11]. The current scheme does not suffer from this difficultly. A solution was obtained for the flow about the leading edge of a semi-infinite parabolic body, shown in Fig. 11. For this case, Dirichlet boundary conditions were used at the far-field, where the velocity field was taken from the incompressible solution given by a conformal mapping around the body. The freestream entropy was specified, and a uniform total enthalpy was computed by taking the freestream Mach number equal to 0.1. A fine grid of 129×129 grid points was computed from the conformal mapping, and 6 grid levels were used. In the symmetric Gauss-Seidel relaxation, it was necessary to underrelax the streamwise sweep with a factor of 0.9 for stability. The wall boundary conditions were simple reflection of the velocity, entropy and pressure.

Pressure coefficient contours are shown Fig. 12, and

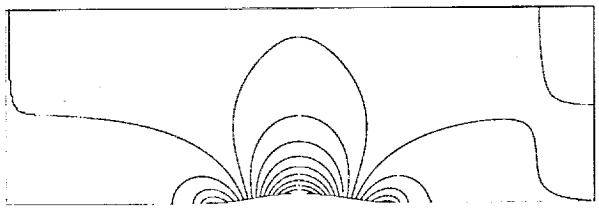

Figure 5. Mach number contours for a $M = 10^{-4}$ inlet, contour increment $\Delta M = 2 \times 10^{-6}$, for a 385×129 grid.

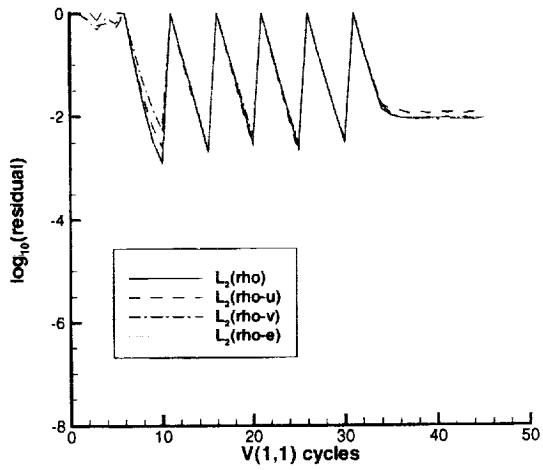

Figure 6. Convergence rates for a $M = 10^{-4}$ inlet flow using a FMG cycle with a 385×129 fine grid.

are seen to be symmetric about the axis of the parabola. Convergence rates are shown in Fig. 13. Unlike the channel flow, the convergence rates are not quite $O(n)$, becoming slightly slower on finer grids. This is because of the underrelaxation of the streamwise Gauss-Seidel sweep, which prevents the advection factor from being solved in that sweep. The asymptotic convergence rate on the finest grid is approximately 0.50 per cycle. The entropy error, Fig. 14, is seen to converge as well as for the channel flow, with a reduction of around one-third with each grid doubling.

Conclusions

A factorizable discretization of the compressible Euler equations on general curvilinear body-fitted grids has been presented. The discretization is based on the multidimensional upwind scheme of Sidilkover, and can be written in a form that is closely related to conventional upwind-differenced finite-volume schemes. Unlike conventional schemes, this discretization lends itself to an extremely efficient multigrid solution procedure. The factorizability of the scheme has the property that the correct incompressible limit of the compressible equations is obtained without the need for any special preconditioning. Because the scheme is stable for Gauss-Seidel relaxation, fast convergence may be obtained for essentially incompressible flow as well as high subsonic Mach numbers. This discretization unifies compressible and incompressible flow algorithms.

References

1. Brandt, A., "Multigrid Techniques: 1984 Guide with Applications to Fluid Dynamics," GMD-Studie 85, GMD-FIT, 1985.
2. Brandt, A., and Yavneh, I., "Accelerated Multigrid Convergence and High-Reynolds Recirculating Flows," *SIAM J. Sci. Statist. Comput.*, vol. 14, no. 3, pp. 607–626, 1993.
3. Ta'asan, S., "Canonical-Variables Multigrid Method for Steady-State Euler Equations," ICASE Report 94-14, 1994.
4. Ta'asan, S., "Canonical Forms of Multidimensional Steady Inviscid Flow," ICASE Report 93-34, 1993.
5. Roberts, T. W., Sidilkover, D., and Swanson, R. C., "Textbook Multigrid Efficiency for the Steady Euler Equations," *AIAA Paper* 97-1949, 1997.
6. Roberts, T. W., Swanson, R. C., and Sidilkover, D., "An Algorithm for Ideal Multigrid Convergence for the Steady Euler Equations," *Computers and Fluids*, vol. 28, nos. 4-5, pp. 427–442, 1999.
7. Sanchez, J., "An Optimally Converging Multigrid Algorithm for the Three-Dimensional Euler Equations," M.Sc. thesis, George Washington University, 1998.
8. Sidilkover, D., "Factorizable Schemes for the Equations of Fluid Flow," ICASE Report 99-20, 1999.

9. Sidilkover, D., "A Genuinely Multidimensional Upwind Scheme and Efficient Multigrid Solver for the Compressible Euler Equations," ICASE Report 94–84, 1994.

10. Sidilkover, D., "Some approaches towards constructing optimally efficient multigrid solvers for the inviscid flow equations," *Computers and Fluids*, vol. 28, nos. 4–5, pp. 551–557, 1999.

11. Roberts, T. W., Swanson, R. C., "Extending Ideally Converging Multigrid Methods to Airfoil Flows," *AIAA Paper* 99-3337, 1999.

12. Sidilkover, D., "Factorizable Schemes for the Steady-State Equations of Compressible Fluid Flow in Two and Three Dimensions,", ICASE Report in preparation.

Appendix: Discretization of D_{HO}

The discretization of the derivatives in the expression for D_{HO}, given in Eqs. (13) must be done in a very precise was so as to preserve the factorizability of the discrete scheme. In Ref. 12, Sidilkover presents these expressions for a uniform Cartesian grid. The particular case of $|\bar{U}| > |\bar{V}|$ is presented here. In this case, D_{HO} is given by Eq. (13a), repeated here for convenience.

$$D_{\mathrm{HO}} \equiv D + \frac{1}{2}\mathrm{sgn}\bar{U}\,\bar{V}\left(\partial_\eta \bar{U} + \partial_\xi \bar{V}\right) - \frac{1}{2}|\bar{V}|\left(1 - \left|\frac{\bar{V}}{\bar{U}}\right|\right)\partial_\eta \bar{V}$$

The term D has already been discussed in the Discretization section, and what remains is $\partial_\eta \bar{U}$, $\partial_\xi \bar{V}$ and $\partial_\eta \bar{V}$ above. Each of these terms is discretized differently on a ξ-cell edge, $(i \pm 1/2, j)$, and an η-cell edge, $(i, j \pm 1/2)$, where i and j are the indices of the vertices in the ξ and η directions, respectively.

Consider the ξ-cell edge, $(i+1/2, j)$. First we take $\bar{U} > 0, \bar{V} > 0$, in which case the following difference formulas are used.

$$\partial_\eta^h \bar{U} = \frac{1}{2}\left(\bar{U}_{i,j} - \bar{U}_{i,j-2}\right),$$
$$\partial_\xi^h \bar{V} = \frac{1}{2}\left(\bar{V}_{i,j} + \bar{V}_{i,j-1} - \bar{V}_{i-1,j} - \bar{V}_{i-1,j-1}\right),$$
$$\partial_\eta^h \bar{V} = \frac{1}{2}\left(\bar{V}_{i-1,j+1} - \bar{V}_{i-1,j-1}\right).$$

Second, take $\bar{U} > 0, \bar{V} < 0$.

$$\partial_\eta^h \bar{U} = \frac{1}{2}\left(\bar{U}_{i,j+2} - \bar{U}_{i,j}\right),$$
$$\partial_\xi^h \bar{V} = \frac{1}{2}\left(\bar{V}_{i,j+1} + \bar{V}_{i,j} - \bar{V}_{i-1,j+1} - \bar{V}_{i-1,j}\right),$$
$$\partial_\eta^h \bar{V} = \frac{1}{2}\left(\bar{V}_{i-1,j+1} - \bar{V}_{i-1,j-1}\right).$$

Third, take $\bar{U} < 0, \bar{V} > 0$.

$$\partial_\eta^h \bar{U} = \frac{1}{2}\left(\bar{U}_{i+1,j} - \bar{U}_{i+1,j-2}\right),$$
$$\partial_\xi^h \bar{V} = \frac{1}{2}\left(\bar{V}_{i+2,j} + \bar{V}_{i+2,j-1} - \bar{V}_{i+1,j} - \bar{V}_{i+1,j-1}\right),$$
$$\partial_\eta^h \bar{V} = \frac{1}{2}\left(\bar{V}_{i+2,j+1} - \bar{V}_{i+2,j-1}\right).$$

Fourth, take $\bar{U} < 0, \bar{V} < 0$.

$$\partial_\eta^h \bar{U} = \frac{1}{2}\left(\bar{U}_{i+1,j+2} - \bar{U}_{i+1,j}\right),$$
$$\partial_\xi^h \bar{V} = \frac{1}{2}\left(\bar{V}_{i+2,j+1} + \bar{V}_{i+2,j} - \bar{V}_{i+1,j+1} - \bar{V}_{i+1,j}\right),$$
$$\partial_\eta^h \bar{V} = \frac{1}{2}\left(\bar{V}_{i+2,j+1} - \bar{V}_{i+2,j-1}\right).$$

Now consider the η-cell edge, $(i, j+1/2)$. First we take $\bar{U} > 0, \bar{V} > 0$, in which case the following difference formulas are used.

$$\partial_\eta^h \bar{U} = \frac{1}{2}\left(\bar{U}_{i,j} - \bar{U}_{i,j-1} + \bar{U}_{i-1,j} - \bar{U}_{i-1,j-1}\right),$$
$$\partial_\xi^h \bar{V} = \frac{1}{2}\left(\bar{V}_{i,j} - \bar{V}_{i-2,j}\right),$$
$$\partial_\eta^h \bar{V} = \frac{1}{2}\left(\bar{V}_{i-1,j+1} - \bar{V}_{i-1,j} + \bar{V}_{i-2,j+1} - \bar{V}_{i-2,j}\right).$$

Second, take $\bar{U} > 0, \bar{V} < 0$.

$$\partial_\eta^h \bar{U} = \frac{1}{2}\left(\bar{U}_{i,j+2} - \bar{U}_{i,j+1} + \bar{U}_{i-1,j+2} - \bar{U}_{i-1,j+1}\right),$$
$$\partial_\xi^h \bar{V} = \frac{1}{2}\left(\bar{V}_{i,j+1} - \bar{V}_{i-2,j+1}\right),$$
$$\partial_\eta^h \bar{V} = \frac{1}{2}\left(\bar{V}_{i-1,j+1} - \bar{V}_{i-1,j} + \bar{V}_{i-2,j+1} - \bar{V}_{i-2,j}\right).$$

Third, take $\bar{U} < 0, \bar{V} > 0$.

$$\partial_\eta^h \bar{U} = \frac{1}{2}\left(\bar{U}_{i+1,j} - \bar{U}_{i+1,j-1} + \bar{U}_{i,j} - \bar{U}_{i,j-1}\right),$$
$$\partial_\xi^h \bar{V} = \frac{1}{2}\left(\bar{V}_{i+2,j} - \bar{V}_{i,j}\right),$$
$$\partial_\eta^h \bar{V} = \frac{1}{2}\left(\bar{V}_{i+2,j+1} - \bar{V}_{i+2,j} + \bar{V}_{i+2,j+1} - \bar{V}_{i+1,j}\right).$$

Fourth, take $\bar{U} < 0, \bar{V} < 0$.

$$\partial_\eta^h \bar{U} = \frac{1}{2}\left(\bar{U}_{i+1,j+2} - \bar{U}_{i+1,j+1} + \bar{U}_{i,j+2} - \bar{U}_{i,j+1}\right),$$
$$\partial_\xi^h \bar{V} = \frac{1}{2}\left(\bar{V}_{i+2,j+1} - \bar{V}_{i,j+1}\right),$$
$$\partial_\eta^h \bar{V} = \frac{1}{2}\left(\bar{V}_{i+2,j+1} - \bar{V}_{i+2,j} + \bar{V}_{i+2,j+1} - \bar{V}_{i+1,j}\right).$$

The above differences are also the ones used in the definition of the second-order advection operator $\mathbf{q}_{\mathrm{HO}}$. Analogous expressions may be developed for Eq. (13b), corresponding to $|\bar{V}| > |\bar{U}|$.

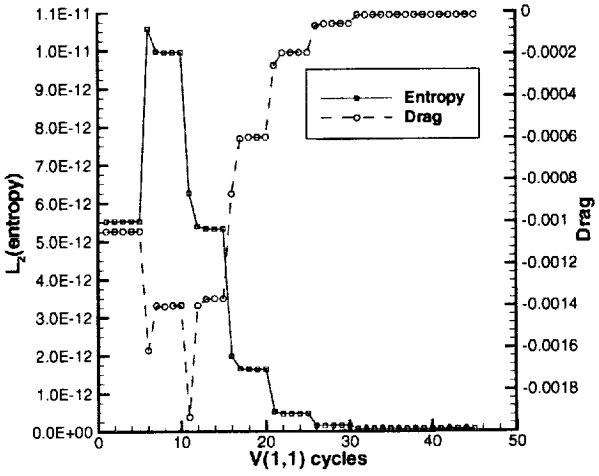

Figure 7. Convergence of the L_2 entropy error and drag on the lower wall for a $M = 10^{-4}$ inlet flow using a FMG cycle with a 385×129 fine grid.

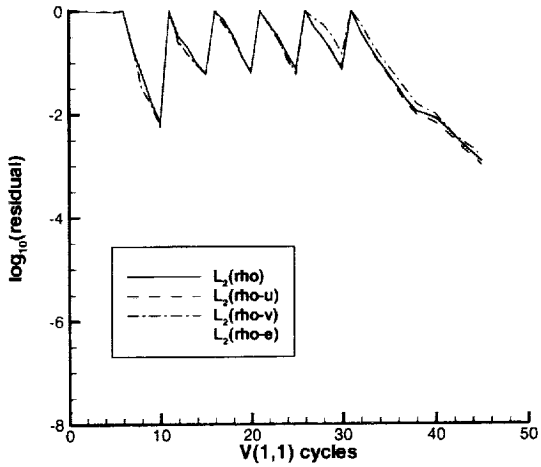

Figure 9. Convergence rates for a $M = 0.73$ inlet flow using a FMG cycle with a 385×129 fine grid.

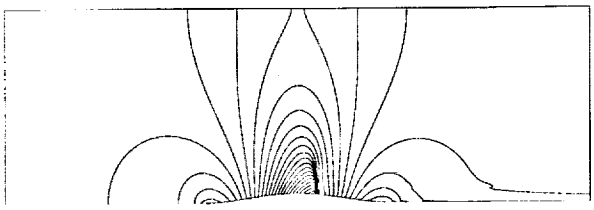

Figure 8. Mach number contours for a $M = 0.73$ inlet, contour increment $\Delta M = 0.025$, for a 385×129 grid.

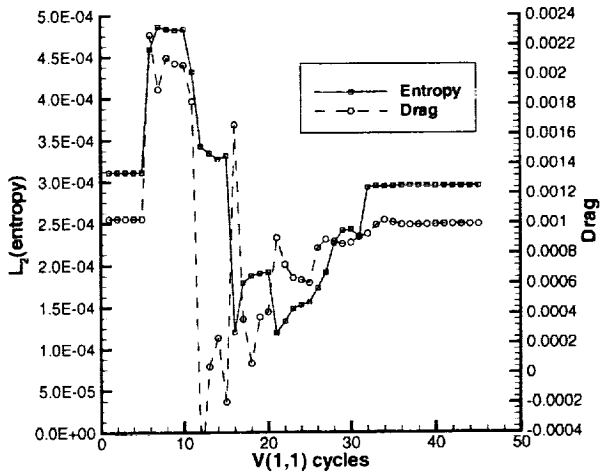

Figure 10. Convergence of the L_2 entropy error and drag on the lower wall for a $M = 0.73$ inlet flow using a FMG cycle with a 385×129 fine grid.

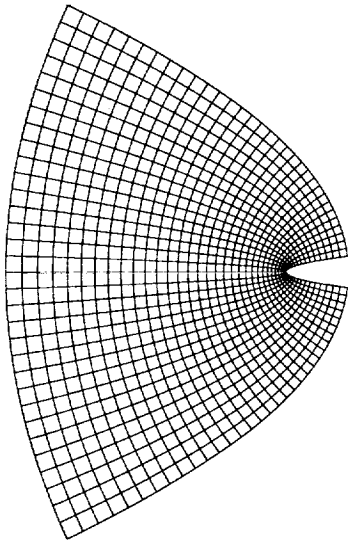

Figure 11. Semi-infinite parabola, 33×33 grid.

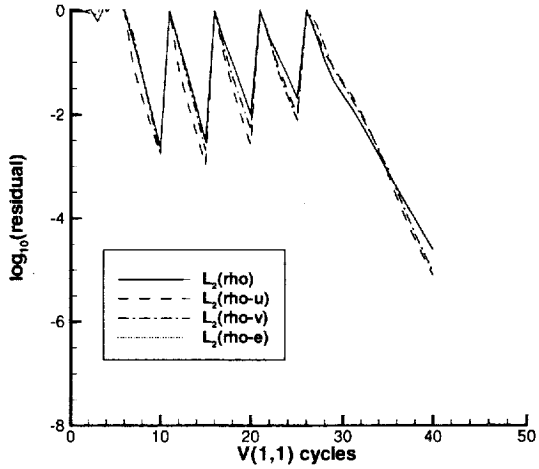

Figure 13. Convergence rates for a $M = 0.1$ leading-edge using a FMG cycle with a 129×129 fine grid.

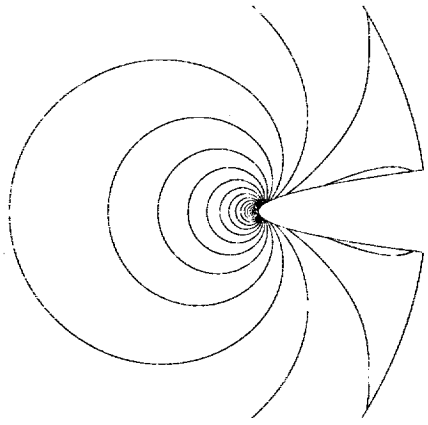

Figure 12. Pressure coefficient contours around a $M = 0.1$ leading-edge, increment $\Delta C_p = 0.05$, for a 129×129 grid.

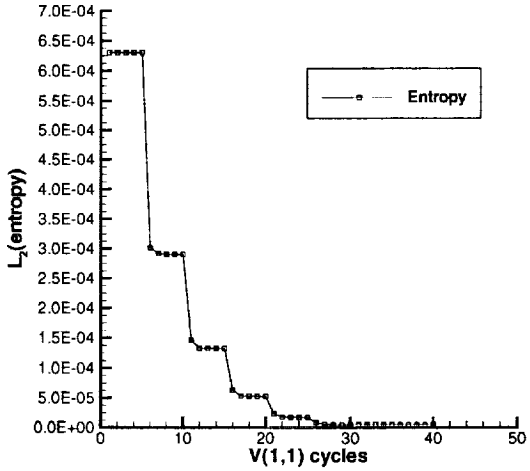

Figure 14. Convergence of the L_2 entropy error for a $M = 0.1$ leading-edge flow using a FMG cycle with a 129×129 fine grid.